Journal of Engineering Mathematics **49:** 163–180, 2004.

A finite-element method for interfacial surfactant transport, with application to the flow-induced deformation of a viscous drop

C. POZRIKIDIS
Department of Mechanical and Aerospace Engineering, University of California, San Diego, La Jolla, California 92093-0411, USA (e-mail: cpozrikidis@ucsd.edu)

Received 25 February 2003; accepted in revised form 4 November 2003

Abstract. A Galerkin finite-element method is developed for solving the transport equation governing the evolution of the surface concentration of an insoluble surfactant over a stationary or evolving fluid interface. The numerical procedure is implemented on an unstructured three-dimensional surface grid consisting of six-node curved triangular elements. Numerical investigations show that the finite-element method is superior to a previously developed finite-volume method for both convection- and diffusion-dominated transport, and especially when the interfacial grid is coarse and steep gradients arise due to local accumulation. The numerical methods for surface transport are combined with a boundary-element method for Stokes flow, and dynamical simulations are performed to illustrate the possibly significant effect of the surface equation of state relating the surface tension to the surfactant concentration on the deformation of a viscous drop in simple shear flow.

Key words: finite-element methods, finite-volume methods, interfacial flow, surface transport, surfactants

1. Introduction

The stability and dynamics of interfaces between two viscous fluids are affected to various degrees by the presence of surfactants, acting to lower the surface tension, and simultaneously generate tangential gradients in the surface tension described as Marangoni tractions. Although in most cases surfactants have a stabilizing influence by lowering the capillary pressure and thus diminishing the intensity of interfacial forces driving an instability, recent work has demonstrated that they may also be responsible for a new mode of instability associated with the Marangoni tractions in gravity-driven film flow and two-layer channel flow [1, 2]. Moreover, surfactants can have a subtle influence on the rheology and stability of dense emulsions and foam [3].

Our ability to describe the precise effect of a surfactant relies to a large extent on the availability of efficient numerical methods for computing interfacial flow and simultaneously solving the transport equation for the surfactant concentration in the bulk of the fluids and over the interfaces. If the surfactant is effectively insoluble, transport occurs only over the interfaces. Although the two-dimensional and axisymmetric versions of the surface transport problem can be tackled efficiently and accurately by standard numerical methods for one-dimensional partial differential equations (*e.g.*, [4]), consideration of the full three-dimensional problem presents challenges typical of those encountered in the computation of three-dimensional scalar or vector fields separated by moving fronts.

Few numerical studies have addressed the effect of surfactants on the three-dimensional deformation of liquid drops and bubbles in a specified incident flow. In Stokes flow, given the instantaneous distribution of the surfactant concentration, the surface tension can be calculated

from a surface equation of state, and the interfacial velocity may be computed by solving an integral equation using well-established boundary-element methods. Once the instantaneous interfacial velocity is available, the surfactant transport equation can be integrated in time using either finite-difference methods in global curvilinear coordinates [5], or finite-volume methods based on an unstructured interfacial grid [6]. Due to numerical difficulties associated with coupling hydrodynamics and interfacial transport, the effect of surfactants on the deformation of drops and bubbles in Navier-Stokes flow appears to have been considered only by Drumright-Clarke and Renardy [7]. Apart from this recent work, numerical simulations using the immersed boundary method or the volume-of-fluid method at non-zero Reynolds numbers have only addressed situations where the interfaces are clean, even for two-dimensional and axisymmetric configurations (*e.g.*, [8]).

Finite-difference methods for solving the surface transport equation over a three-dimensional interface have several shortcomings, including spatially uneven discretization around singular grid points. Finite-volume methods are more efficient but require ad-hoc averaging and heuristic interpolation between the finite-volumes, edges, and nodes. On the other hand, the advantages of finite-element and spectral-element methods regarding accuracy, adaptivity, and convergence are well known (*e.g.*, [9, 10]). A main goal of this paper is to illustrate the implementation of the Galerkin finite-element method for solving the surfactant interface transport equation, and compare its efficiency with a rival finite-volume method. A broader objective is to provide a benchmark that will guide the further development of numerical methods for interfacial flow with capsule-like interfacial properties, such as those encountered in surfactant driven and thermocapillary flows. To the author's knowledge, this is the first time that the finite-element method has been implemented for solving a transport equation over an evolving three-dimensional surface.

Numerical experiments will reveal that the finite-element method is significantly more accurate than the finite-volume method implemented in previous work, especially when a coarse grid is employed. On the physical side, numerical simulations will illustrate the possibly important effect of the surface equation of state on the deformation of a low-viscosity drop in simple shear flow.

2. Governing equations

Consider an evolving interface between two immiscible viscous fluids occupied by an insoluble surfactant. It is both kinematically consistent and computationally beneficial to regard the interface as being composed of a continuous distribution of marker points moving with the velocity of the fluid normal to the interface, $u_n\,\mathbf{n}$, and with an arbitrary tangential component, $\mathbf{w}$, as illustrated in Figure 1, where $u_n \equiv \mathbf{u}\cdot\mathbf{n}$, $\mathbf{n}$ is the unit normal vector, and $\mathbf{u}$ is the fluid velocity. In the finite-element literature, endowing the marker points with the freedom to move with an arbitrary tangential velocity is known as the arbitrary Lagrangian-Eulerian formulation (ALE) (*i.e.*, [10, pp. 8–13]). The marker-point velocity may thus be expressed in the general form

$$\mathbf{v} = u_n\,\mathbf{n} + \mathbf{w}. \tag{2.1}$$

If the marker points are chosen to be material (Lagrangian) point particles moving with the fluid velocity, then

$$\mathbf{w} = \mathbf{u}_s \equiv \mathbf{n}\times(\mathbf{u}\times\mathbf{n}) = \mathbf{P}\cdot\mathbf{u} \qquad \text{and} \qquad \mathbf{v} = \mathbf{u}, \tag{2.2}$$

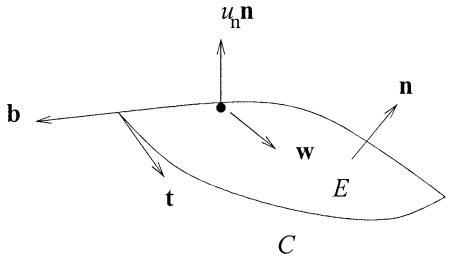

Figure 1. Schematic illustration of a section of an interface. Interfacial marker points move with the normal component of the fluid velocity, u_n **n**, and an arbitrary tangential component **w**.

where $\mathbf{u}_s$ is the "surface" or tangential velocity, $\mathbf{P} = \mathbf{I} - \mathbf{nn}$ is the tangential projection operator, and **I** is the identity matrix. On the other hand, if the marker points move with the normal component of the fluid velocity, $\mathbf{w} = \mathbf{0}$ and $\mathbf{v} = u_n\,\mathbf{n}$.

Performing a surfactant mass balance over an infinitesimal section of the interface, we find that the evolution of the surface concentration of the surfactant, Γ, measured in moles per surface area, is governed by a convection–diffusion equation in the presence of a distributed source,

$$\frac{\mathrm{d}\Gamma}{\mathrm{d}t} + (\mathbf{u}_s - \mathbf{w}) \cdot \nabla_s \Gamma + \Gamma\,\theta_s = D_s\,\nabla_s^2 \Gamma, \tag{2.3}$$

where $\nabla_s \equiv \mathbf{P} \cdot \nabla$ is the surface gradient, and D_s is the surfactant surface diffusivity [5, 6]. The derivative $\mathrm{d}/\mathrm{d}t$ on the left-hand side of (2.3) expresses the rate of change of a variable following an interfacial marker point moving with the velocity stated in (2.1); when the marker points are Lagrangian point particles, $\mathrm{d}/\mathrm{d}t$ reduces to the material derivative usually denoted by $\mathrm{D}/\mathrm{D}t$. The third term on the left-hand side of (2.3) expresses the effect of the rate of surface dilatation, given by

$$\theta_s \equiv \nabla_s \cdot \mathbf{u} = \text{Trace}\,[\mathbf{P} \cdot (\nabla \mathbf{u}) \cdot \mathbf{P}] = \nabla_s \cdot \mathbf{u}_s + 2\,\kappa_m\,u_n, \tag{2.4}$$

where $2\kappa_m = \nabla_s \cdot \mathbf{n}$, and κ_m is the mean curvature. The first term on the right-hand side of (2.4), equal to the surface divergence of the tangential velocity, expresses dilatation due to in-plane stretching, whereas the second term expresses dilatation by expansion due to normal motion. In the particular case of an expanding sphere, only the second term survives. In numerical practice, the rate of surface dilatation may be computed conveniently from the expression

$$\theta_s = \frac{1}{h_s}\left(\frac{\partial \mathbf{u}}{\partial \xi} \times \frac{\partial \mathbf{x}}{\partial \eta} + \frac{\partial \mathbf{x}}{\partial \xi} \times \frac{\partial \mathbf{u}}{\partial \eta}\right) \cdot \mathbf{n}, \tag{2.5}$$

where (ξ, η) are right-handed surface curvilinear coordinates, $h_s = |\partial \mathbf{x}/\partial \xi \times \partial \mathbf{x}/\partial \eta|$ is the surface metric defined by the differential relation $\mathrm{d}S = h_s\,\mathrm{d}\xi\,\mathrm{d}\eta$, and $\mathrm{d}S$ is the area of an infinitesimal surface element ([13, p. 17]).

An alternative form of the transport equation (2.3) is

$$\frac{\mathrm{d}\Gamma}{\mathrm{d}t} + \nabla_s \cdot (\Gamma\,\mathbf{u}_s) - \mathbf{w} \cdot \nabla_s \Gamma + \Gamma\,2\,\kappa_m\,u_n = D_s\,\nabla_s^2 \Gamma. \tag{2.6}$$

At steady state and when $\mathbf{w} = \mathbf{0}$, the marker points are stationary, all terms but the second on the left-hand side of (2.6) vanish, and the resulting simplified equation, $\nabla_s \cdot (\Gamma\,\mathbf{u}_s) = D_s\,\nabla_s^2 \Gamma$, expresses a balance between convection and diffusion over the stationary interface.

The alternative form (2.6) is motivated by the presence of the surface divergence on the left-hand side, allowing us to apply the surface divergence theorem in developing the finite-volume and finite-element methods, as will be discussed in Sections 4 and 5.

When the surfactant concentration is below the saturation level, a linear relationship may be assumed between the surface tension and the surfactant surface concentration according to Gibbs, $\gamma_c - \gamma = \Gamma RT$, where R is the ideal gas constant, T is the absolute temperature, and γ_c is the surface tension of a clean interface that is devoid of surfactants [11]. Rearranging, we obtain the linear law

$$\gamma = \gamma_c \left(1 - \beta \frac{\Gamma}{\Gamma_0}\right) = \frac{\gamma_0}{1-\beta} \left(1 - \beta \frac{\Gamma}{\Gamma_0}\right), \tag{2.7}$$

where $\beta = \Gamma_0 RT/\gamma_c$ is a dimensionless constant related to the surface elasticity, $E \equiv -\partial\gamma/\partial\Gamma$, by $E = \gamma_c\beta/\Gamma_0$, and Γ_0 is a reference surfactant concentration corresponding to the surface tension $\gamma_0 = \gamma_c\,(1-\beta)$. The effect of the surfactant can be expressed either by the dimensionless coefficient β or by the Marangoni number $\mathrm{Ma} \equiv E\Gamma_0/\gamma_0 = \beta/(1-\beta)$.

More generally, the relationship between surface tension and surfactant concentration is nonlinear, that is, the surface elasticity is a function of the local concentration. For small variations in the surfactant concentration around the reference value Γ_0, we obtain Henry's equation of state expressed by $\gamma = \gamma_0 - E\,(\Gamma - \Gamma_0)$, where $E = -(\partial\gamma/\partial\Gamma)_{\Gamma_0}$. For large variations, we may use Langmuir's equation of state

$$\begin{aligned} \gamma &= \gamma_c + RT\Gamma_\infty \log\left(1 - \frac{\Gamma}{\Gamma_\infty}\right) = \gamma_c \left[1 + \frac{\beta}{\psi} \log\left(1 - \psi \frac{\Gamma}{\Gamma_0}\right)\right] \\ &= \frac{\gamma_0}{1 + \frac{\beta}{\psi}\log(1-\psi)} \left[1 + \frac{\beta}{\psi} \log\left(1 - \psi \frac{\Gamma}{\Gamma_0}\right)\right], \end{aligned} \tag{2.8}$$

applicable for second-order adsorption/desorption kinetics; Γ_∞ is the maximum surface packing surfactant concentration, and $\psi = \Gamma_0/\Gamma_\infty$ is the surface coverage at the reference state [12]. In deriving Langmuir's equation of state, ideal behavior has been assumed to neglect cohesive and repulsive interactions between the surfactant molecules arranged in a monolayer.

The surfactant transport equation, the surface equation of state, and the equations describing the hydrodynamics on either side of the interface are strongly coupled through the dynamic interfacial condition for the jump in the hydrodynamic traction, $\Delta\mathbf{f}$,

$$\Delta\mathbf{f} \equiv (\boldsymbol{\sigma}^{(1)} - \boldsymbol{\sigma}^{(2)}) \cdot \mathbf{n} = 2\kappa_m\,\gamma\,\mathbf{n} - \nabla_s\gamma, \tag{2.9}$$

where $\boldsymbol{\sigma}^{(j)}$ is the stress tensor for the jth fluid on either side of the interface, $j = 1, 2$, and the normal vector $\mathbf{n}$ is reckoned to point into fluid 1. In line with the main objective of this paper, we shall heretoforth assume that a method for computing the hydrodynamics is available, and shall concentrate on numerical methods for solving the surfactant transport equation by numerical methods.

3. Surface discretization and interpolation

To describe the interface in numerical form, we introduce a surface grid consisting of six-node curved triangular elements, as depicted in Figure 2. The parametric representation is implemented by mapping each curved triangle from the physical three-dimensional space to a

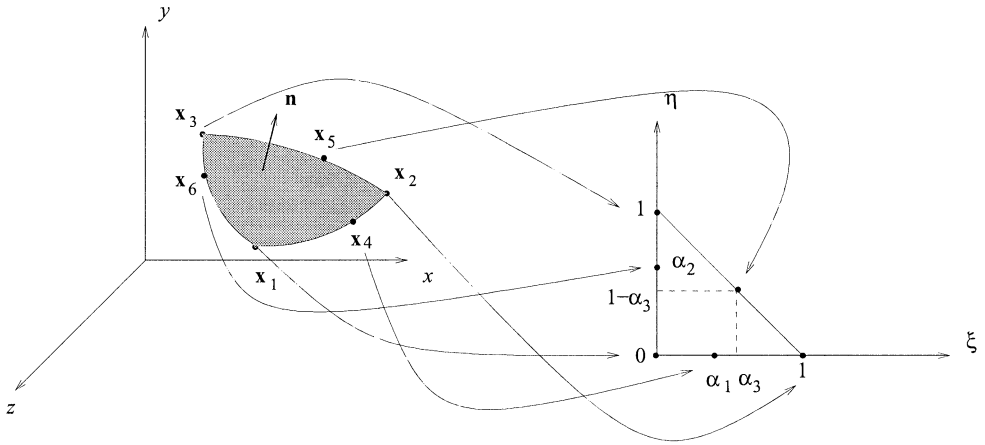

Figure 2. A quadratic triangular element is defined by 3 vertex nodes and 3 mid-nodes, a total of 6 nodes. In the parametric representation, the curved triangle is mapped to a right isosceles triangle in the parametric (ξ, η)-plane.

right isosceles triangle in the parametric (ξ, η)-plane, as shown in Figure 2. The first element node is mapped to the origin, the second is mapped to the point $\xi = 1, \eta = 0$ on the ξ-axis, the third is mapped to the point $\xi = 0, \eta = 1$ on the η-axis, the fourth is mapped to the point $\xi = \alpha_1, \eta = 0$, the fifth is mapped to the point $\xi = \alpha_3, \eta = 1 - \alpha_3$, and the sixth is mapped to the point $\xi = 0, \eta = \alpha_2$.

The mapping of an arbitrary surface point that lies on the mapper triangle is mediated by the function

$$\mathbf{x} = \sum_{i=1}^{6} \mathbf{x}_i \, \psi_i(\xi, \eta), \tag{3.1}$$

where $\mathbf{x}_i$ are the element node positions, $\psi(\xi, \eta)$ are local element-node cardinal interpolation functions given by

$$\begin{aligned}
\psi_2 &= \frac{1}{1-\alpha_1}\,\xi\,\left(\xi - \alpha_1 + \frac{\alpha_1 - \alpha_3}{1-\alpha_3}\,\eta\right),\\
\psi_3 &= \frac{1}{1-\alpha_2}\,\eta\,\left(\eta - \alpha_2 + \frac{\alpha_2 + \alpha_3 - 1}{\alpha_3}\,\xi\right),\\
\psi_4 &= \frac{1}{\alpha_1(1-\alpha_1)}\,\xi\,(1-\xi-\eta),\\
\psi_5 &= \frac{1}{\alpha_3(1-\alpha_3)}\,\xi\,\eta,\\
\psi_6 &= \frac{1}{\alpha_2(1-\alpha_2)}\,\eta\,(1-\xi-\eta),\\
\psi_1 &= 1 - \psi_2 - \psi_3 - \psi_4 - \psi_5 - \psi_6,
\end{aligned} \tag{3.2}$$

and

$$\alpha_1 = \frac{1}{1 + \frac{|\mathbf{x}_4 - \mathbf{x}_2|}{|\mathbf{x}_4 - \mathbf{x}_1|}}, \qquad \alpha_2 = \frac{1}{1 + \frac{|\mathbf{x}_6 - \mathbf{x}_3|}{|\mathbf{x}_6 - \mathbf{x}_1|}}, \qquad \alpha_3 = \frac{1}{1 + \frac{|\mathbf{x}_5 - \mathbf{x}_2|}{|\mathbf{x}_5 - \mathbf{x}_3|}} \tag{3.3}$$

are dimensionless geometrical parameters. The normal vector and mean curvature are computed from the parametric representation using standard formulas of differential geometry (*e.g.*, [13, Section 1.5]).

In the isoparametric representation adopted in this work, the counterparts of (3.1) is applied for all geometrical and physical surface functions of interest, such as the mean curvature or the surface concentration of the surfactant.

4. Finite-volume method

The surfactant transport equations (2.3) and (2.6) can be integrated in time using an implementation of the finite-volume method (FVM) developed by Yon and Pozrikidis [6]. For completeness, a brief outline of this method will be given in this section.

We begin by integrating Equations (2.3) and (2.6) over the surface of an element E that is bounded by the contour C, and use the surface divergence theorem to find, respectively,

$$\int_E \frac{\mathrm{d}\Gamma}{\mathrm{d}t}\,\mathrm{d}S + \int_E (\mathbf{u}_s - \mathbf{w})\cdot\nabla_s\Gamma\,\mathrm{d}S + \int_E \Gamma\,\theta_s\,\mathrm{d}S = D_s\int_C \mathbf{b}\cdot\nabla_s\Gamma\,\mathrm{d}l, \tag{4.1}$$

and

$$\int_E \frac{\mathrm{d}\Gamma}{\mathrm{d}t}\,\mathrm{d}S + \int_C \Gamma\,\mathbf{b}\cdot\mathbf{u}\,\mathrm{d}l - \int_E \mathbf{w}\cdot\nabla_s\Gamma\,\mathrm{d}S + \int_E \Gamma\,2\kappa_m\,u_n\,\mathrm{d}S = D_s\int_C \mathbf{b}\cdot\nabla_s\Gamma\,dl, \tag{4.2}$$

where $\mathbf{b} = \mathbf{t}\times\mathbf{n}$ is the unit vector that is tangential to the interface and normal to the element contour C, as shown in Figure 1, $\mathbf{t}$ is the unit vector tangential to C, and l is the arc length along C.

Consider (4.1) with $\mathbf{w} = \mathbf{u}_s$, in which case the marker points move with the fluid velocity. Approximating Γ with a constant function termed the "element value" inside the first and third integrals on the left-hand side and rearranging, we obtain

$$\frac{\mathrm{d}\Gamma^E}{\mathrm{d}t} = -\frac{\Gamma^E}{S_E}\int_E \theta_s\,\mathrm{d}S + \frac{D_s}{S_E}\int_C \mathbf{b}\cdot\nabla_s\Gamma\,\mathrm{d}l, \tag{4.3}$$

where S_E is the element surface area.

Consider now (4.2) with $\mathbf{w} = \mathbf{0}$, in which case the marker points move with the normal component of the fluid velocity. Approximating Γ with a constant function inside the first and fourth integrals on the left-hand side and rearranging, we obtain

$$\frac{\mathrm{d}\Gamma^E}{\mathrm{d}t} = -\frac{\Gamma^E}{S_E}\int_E 2\,\kappa_m\,u_n\,\mathrm{d}S + \frac{1}{S_E}\int_C \mathbf{b}\cdot(-\Gamma\,\mathbf{u} + D_s\,\nabla_s\Gamma)\,\mathrm{d}l. \tag{4.4}$$

The contour integral on the right-hand side incorporates the convective and diffusive fluxes across the element contour C.

Equations (4.3) and (4.4) were discretized and integrated in time using the numerical method developed in the earlier work [6]. Compiling the evolution equations for all elements, $i = 1, \ldots, N_E$, and evaluating the integrands of the element integrals by isoparametric interpolation in terms of the velocity and surfactant concentration of the surfactant at the nodes,

we obtain a coupled linear system of ODEs for the element values,

$$\frac{\mathrm{d}\Gamma_i^E}{\mathrm{d}t} = \sum_{j=1}^{N_E} A_{ij}(t)\,\Gamma_j^E, \tag{4.5}$$

where the matrix **A** is defined in terms of the surface velocity at the nodes. In practice, the surface integration over the elements is performed in the parametric (ξ, η)-plane using a 6-point quadrature for the triangle [14]. To compute the matrix **A**, we use the method of impulses: denoting the right-hand side of (4.3) or (4.4) for the ith element by R_i, we set $A_{ij} = R_i(\Gamma_1 = 0, \ldots, \Gamma_{j-1} = 0, \Gamma_j = 1, \Gamma_{j+1} = 0, \cdots, \Gamma_{N_E} = 0)$.

Discretizing (4.5) according to the fully-implicit Crank-Nicolson method, we obtain

$$\frac{\Gamma_i^E(t+\Delta t) - \Gamma_i^E(t)}{\Delta t} = \frac{1}{2}\sum_{j=1}^{N_E} A_{ij}(t)\,[\,\Gamma_j^E(t+\Delta t) + \Gamma_j^E(t)\,], \tag{4.6}$$

and rearrange to derive the $N_E \times N_E$ linear system

$$\sum_{j=1}^{N_E}[\delta_{ij} - \frac{\Delta t}{2}\,A_{ij}(t)\,]\Gamma_j^E(t+\Delta t) = \sum_{j=1}^{N_E}[\delta_{ij} + \frac{\Delta t}{2}\,A_{ij}(t)\,]\Gamma_j^E(t). \tag{4.7}$$

Note that this discretization is second-order accurate in the time step Δt only if the velocity field is independent of time. In the simulations presented in Section 6, the solution of the linear system at every step is found by the method of Gauss elimination with row pivoting.

Once the element values at the new time level are available, the ith nodal value is updated using the formula

$$\Gamma_i = \sum_j \frac{\Gamma_j^E}{d_{ij}} \Big/ \sum \frac{1}{d_{ij}}, \tag{4.8}$$

where the sum in j runs over all elements sharing the ith node, and d_{ij} is the distance of the ith node from the jth element surface centroid.

5. Finite-element method

Alternatively, the surfactant transport equations (2.3) and (2.6) can be integrated in time using the Galerkin finite-element method (GFEM). To implement the method, we express the interfacial surfactant concentration in terms of the nodal values Γ_j and associated global interpolation functions ϕ_j defined over the interface, as

$$\Gamma = \sum_{j=1}^{N_N} \Gamma_j\,\phi_j, \tag{5.1}$$

where N_N is the total number of surface nodes. Next, we multiply the surfactant transport equation (2.3) by ϕ_i, integrate over the interface, use the surface divergence theorem to manipulate the integral of the surface Laplacian on the right-hand side, and substitute expansion

(5.1), to derive the Galerkin finite-element equation

$$\sum_{j=1}^{N_N} \left(\int_D \phi_i \, \phi_j \, \mathrm{d}S \right) \frac{\mathrm{d}\Gamma_j}{\mathrm{d}t} + \sum_{j=1}^{N_N} \left(\int_D \phi_i \, (\mathbf{u}_s - \mathbf{w}) \cdot \nabla_s \phi_j \, \mathrm{d}S \right) \Gamma_j$$
$$+ \sum_{j=1}^{N_N} \left(\int_D \phi_i \, \phi_j \, \theta_s \, \mathrm{d}S \right) \Gamma_j = -D_s \sum_{j=1}^{N_N} \left(\int_D \nabla_s \phi_i \cdot \nabla_s \phi_j \, \mathrm{d}S \right) \Gamma_j. \tag{5.2}$$

Working in a similar fashion with the alternative form (2.6), using this time the divergence theorem to manipulate the integral of the surface Laplacian as well as the integral of the second term on the left-hand side, we find

$$\sum_{j=1}^{N_N} \left(\int_D \phi_i \, \phi_j \, \mathrm{d}S \right) \frac{\mathrm{d}\Gamma_j}{\mathrm{d}t} - \sum_{j=1}^{N_N} \left(\int_D (\mathbf{u}_s \cdot \nabla_s \phi_i) \, \phi_j \, \mathrm{d}S \right) \Gamma_j$$
$$- \sum_{j=1}^{N_N} \left(\int_D \mathbf{w} \cdot (\phi_i \, \nabla_s \phi_j) \, \mathrm{d}S \right) \Gamma_j + \sum_{j=1}^{N_N} \left(\int_D 2 \, \kappa_m \, u_n \, \phi_i \, \phi_j \, \mathrm{d}S \right) \Gamma_j$$
$$= -D_s \sum_{j=1}^{N_N} \left(\int_D \nabla_s \phi_i \cdot \nabla_s \phi_j \, \mathrm{d}S \right) \Gamma_j. \tag{5.3}$$

To derive the corresponding matrix forms, we introduce the global surface mass, advection, and diffusivity matrices

$$M_{ij} \equiv \int_D \phi_i \, \phi_j \, \mathrm{d}S, \qquad N_{ij} \equiv \int_D (\mathbf{u}_s \cdot \nabla_s \phi_i) \, \phi_j \, \mathrm{d}S, \qquad K_{ij} \equiv \int_D \nabla_s \phi_i \cdot \nabla_s \phi_j \, \mathrm{d}S, \tag{5.4}$$

and the weighted mass matrices

$$M^{\theta}_{ij} \equiv \int_D \theta_s \, \phi_i \, \phi_j \, \mathrm{d}S, \qquad M^{\kappa}_{ij} \equiv \int_D 2\kappa_m \, u_n \, \phi_i \, \phi_j \, \mathrm{d}S. \tag{5.5}$$

Details on the computation of these matrices will be given in Section 5.1. The Galerkin finite-element equations (5.2) and (5.3) may then be expressed in the form

$$\sum_{j=1}^{N_N} M_{ij} \, \frac{\mathrm{d}\Gamma_j}{\mathrm{d}t} = \sum_{j=1}^{N_N} B_{ij} \, \Gamma_j, \tag{5.6}$$

where the coefficient matrix B_{ij} depends on the chosen policy of marker point motion.

Selecting (5.2) with $\mathbf{w} = \mathbf{u}_s$, in which case the nodes move with the fluid velocity, we obtain the symmetric form

$$B_{ij} = -M^{\theta}_{ij} - D_s \, K_{ij}. \tag{5.7}$$

On the other hand, selecting (5.3) with $\mathbf{w} = \mathbf{0}$, in which case the nodes move with the normal component of the fluid velocity, we obtain the non-symmetric form

$$B_{ij} = N_{ij} - M^{\kappa}_{ij} - D_s \, K_{ij}. \tag{5.8}$$

Implicit discretization of (5.6) according to the Crank-Nicolson method provides us with the $N_N \times N_N$ linear algebraic system

$$\sum_{j=1}^{N_N}[M_{ij} - \frac{\Delta t}{2}\, B_{ij}(t)\ ]\,\Gamma_j(t+\Delta t) = \sum_{j=1}^{N_N}[M_{ij} + \frac{\Delta t}{2}\, B_{ij}(t)\ ]\,\Gamma_j(t). \tag{5.9}$$

When the coefficient matrix B_{ij} is given by the symmetric form (5.7), the solution of (5.9) can be found expeditiously by the method of Cholesky LL^T or LDL^T decomposition – the former applying to positive-definite matrices – Gauss elimination without pivoting, or conjugate gradients ([14, Chapter 3]). Unfortunately, because in this case the interfacial points are convected with the fluid velocity, severe grid distortion occurs after a certain evolution time, as will be discussed in Section 6.

To ensure the longevity of the simulation, we advect the marker points normal to the interface, and work with the computationally less attractive non-symmetric form (5.8). Direct and iterative numerical methods for solving this more general system are reviewed by Demmel [15]. For simplicity, in the computations presented in this paper, both the symmetric and non-symmetric linear systems were solved by the method of Gauss elimination with row pivoting.

5.1. Computational details

In the numerical implementation, the global matrices (5.4) and (5.5) are assembled from corresponding element matrices involving the six element cardinal interpolation functions, $\psi_j(\xi, \eta)$, given in (3.1). As usual, the correspondence between global and element nodes is made by means of an element-node connectivity table. The surface integrals over the elements are computed over the flat triangle in the parametric (ξ, η)-plane using a 6-point quadrature for the triangle [14]. Isoparametric interpolation is used to evaluate the various surface functions, including the mean curvature, normal component of the fluid velocity, and rate of surface dilatation.

To compute the three-dimensional surface gradients of the element interpolation functions ψ_i, we complement equations

$$\begin{aligned}
\frac{\partial \mathbf{x}}{\partial \xi} \cdot \nabla_s \psi_i &= \sum_{j=1}^{6} \frac{\partial \psi_j}{\partial \xi}\, \mathbf{x}_j^E \cdot \nabla_s \psi_i = \frac{\partial \psi_i}{\partial \xi}, \\
\frac{\partial \mathbf{x}}{\partial \eta} \cdot \nabla_s \psi_i &= \sum_{j=1}^{6} \frac{\partial \psi_j}{\partial \eta}\, \mathbf{x}_j^E \cdot \nabla_s \psi_i = \frac{\partial \psi_i}{\partial \eta},
\end{aligned} \tag{5.10}$$

with the condition

$$\mathbf{n} \cdot \nabla_s \psi_i = 0, \tag{5.11}$$

where the superscript E denotes an element node, and the vector $\mathbf{n}$ is normal to the element. The resulting 3×3 linear takes the form

$$\Pi \cdot \nabla \psi_i = \begin{bmatrix} \partial \psi_i / \partial \xi \\ \partial \psi_i / \partial \eta \\ 0 \end{bmatrix}, \tag{5.12}$$

where

$$\Pi = \left[\begin{array}{c|c|c} \sum_{j=1}^{6} \frac{\partial \psi_j}{\partial \xi}\, x_j^E & \sum_{j=1}^{6} \frac{\partial \psi_j}{\partial \xi}\, y_j^E & \sum_{j=1}^{6} \frac{\partial \psi_j}{\partial \xi}\, z_j^E \\ - - - - - & - - - - & - - - - \\ \sum_{j=1}^{6} \frac{\partial \psi_j}{\partial \eta}\, x_j^E & \sum_{j=1}^{6} \frac{\partial \psi_j}{\partial \eta}\, y_j^E & \sum_{j=1}^{6} \frac{\partial \psi_j}{\partial \eta}\, z_j^E \\ - - - - - & - - - - & - - - - \\ n_x & n_y & n_z \end{array}\right]. \tag{5.13}$$

For a specified value of the pair (ξ, η) lying inside the appropriate range, the solution of (5.12) is found by Cramer's rule.

6. Results and discussion

Several series of simulations were carried out to investigate the performance and compare the efficiency of the numerical methods. In this section, results are presented for a stationary spherical surface with a specified surface velocity field, and for an evolving interface identified with the surface of a viscous drop deforming under the action of a viscous shear flow.

6.1. Transport over a spherical interface

In the first case study, the surfactant transport equation is solved over a spherical surface of radius a, subject to a prescribed axisymmetric tangential velocity field with azimuthal component $u_\theta = \frac{1}{4} V \sin\theta$, as depicted on the left of Figure 3. This velocity field is established over the surface of a viscous drop rising with velocity V through an infinite ambient fluid of same viscosity at low Reynolds numbers, where the motion is observed in a frame of reference where the drop is stationary (*e.g.*, [13, p. 269]).

In the axisymmetric configuration, the surfactant transport equation simplifies to a one-dimensional unsteady convection–diffusion equation with respect to the azimuthal angle θ,

$$\frac{\partial \Gamma}{\partial t} + \frac{1}{a \sin\theta} \frac{\partial}{\partial \theta} (\sin\theta\, u_\theta\, \Gamma) = \frac{D_s}{a^2 \sin\theta} \frac{\partial}{\partial \theta} \left(\sin\theta \frac{\partial \Gamma}{\partial \theta} \right), \tag{6.1}$$

which is to be solved for $0 \le \theta \le \pi$ subject to an initial condition and the regularity condition $\partial\Gamma/\partial\theta = 0$ at $\theta = 0$ and π. The importance of convection relative to diffusion is expressed by the Péclet number, $\mathrm{Pe} = aV/D_s$. At steady state, the solution is given by

$$\Gamma = \frac{A}{4\pi a^2} \frac{\mathrm{Pe}/4}{\sinh(\mathrm{Pe}/4)}\, \exp(-\frac{\mathrm{Pe}}{4}\, \cos\theta), \tag{6.2}$$

where A is the total amount of surfactant. If the initial surfactant concentration is uniform and equal to Γ_0, the first fraction on the right-hand side of (6.2) is also equal to Γ_0.

To provide a point of reference for evaluating the performance of the finite-volume and finite-element methods, the solution of (6.1) was computed on a uniform one-dimensional grid with respect to θ, consisting of 128 spatial divisions. Second-order finite differences were used for approximating of the derivatives with respect to θ, and the Crank-Nicolson method was applied for the time integration, resulting in a tridiagonal algebraic system which is solved by the Thomas algorithm (*e.g.*, [14, Chapter 3]). To screen out the temporal discretization error, the time step was set equal to that used in the finite-volume and finite-element solutions.

Figure 4(*a*) illustrates the evolution of the surfactant concentration from the uniform initial value Γ_0, computed on a coarse three-dimensional grid with 128 elements defined by 258

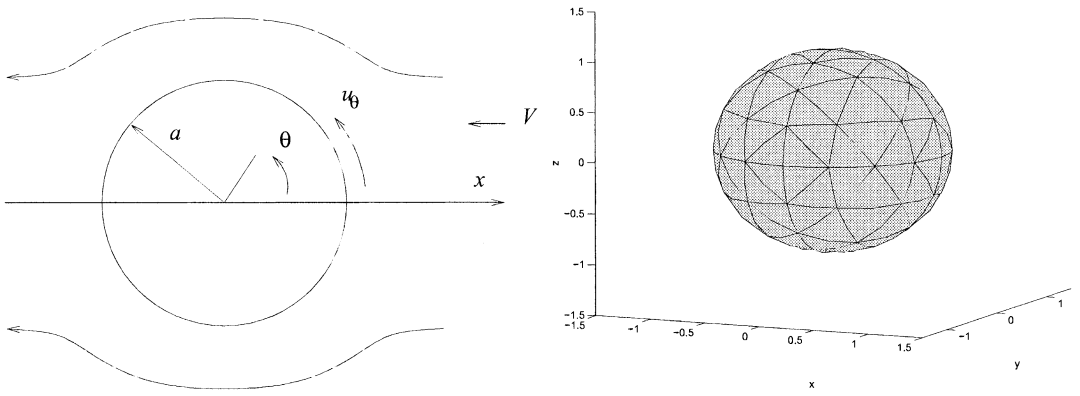

Figure 3. Left: illustration of transport over a spherical surface with a specified tangential velocity field. Right: a coarse surface grid consisting of 128 quadratic elements defined by 258 nodes.

nodes, shown on the right of Figure 3. Figure 4(*b*) shows corresponding results for a fine three-dimensional grid with 512 surface elements defined by 1026 nodes. Both grids descend from the successive subdivision of an octahedron [16]. In both cases, Pe = 10, the time step is $\Delta t = 0{\cdot}10\ a/V$, and the interfacial marker points are kept stationary. The profiles shown in these figures correspond to dimensionless times $tV/a = 0, 2, 4, \ldots, 10$, the last profile being close to the asymptotic distribution established at steady state. The solid lines, squares, and circles connected by dots represent, respectively, results obtained by solving (6.1), by the finite-volume method, and by the finite-element method. The squares and circles correspond to interfacial markers located in the xy meridional plane.

The results show that the finite-element method is superior to the finite-volume method on the coarse grid. To illustrate the behavior of the error in quantitative terms, in Figure 4(*c*) we plot the evolution of the maximum error in the nodal values of the surfactant concentration over the three-dimensional grid, normalized by the instantaneous maximum value of the finite-difference solution occurring at $\theta = \pi$. The pointwise error was computed by interpolating the numerical solution of (6.1) at azimuthal angles corresponding to the position of the interfacial marker points in the three-dimensional grid. At steady state, the error of the finite-volume method on the coarse grid is on the order of 10%, whereas that of the finite-element method is less than 1%. As the grid is refined, the accuracy of both methods improves and differences in the respective numerical solutions become smaller.

The superiority of the finite-element method becomes evident at higher Péclet numbers where the surfactant tends to accumulate inside a narrow axisymmetric cap of angular extent δ around the rear stagnation point. To estimate δ, we introduce the azimuthal angle measured from the rear stagnation point, $\theta' \equiv \pi - \theta$, and specify as a convention that, at $\theta' = \delta$, the surfactant concentration has dropped to 1% of the peak value reached at the rear stagnation point, $\theta' = 0$, Using (6.2), we obtain the estimate

$$\cos\delta \simeq 1 - \frac{18.421}{\mathrm{Pe}}. \tag{6.3}$$

For Pe = 10 and 100, we find, respectively, $\delta/\pi = 0{\cdot}818$ and $0{\cdot}196$. Figure 4(*d*) shows the evolution of the surfactant concentration computed on the coarse grid for Pe = 100, corresponding to low surface diffusivity. The profiles shown correspond to dimensionless times $tV/a = 0, 4{\cdot}0, 8{\cdot}0, \ldots, 20{\cdot}0$. In this case, the finite-volume method fails at an early stage of

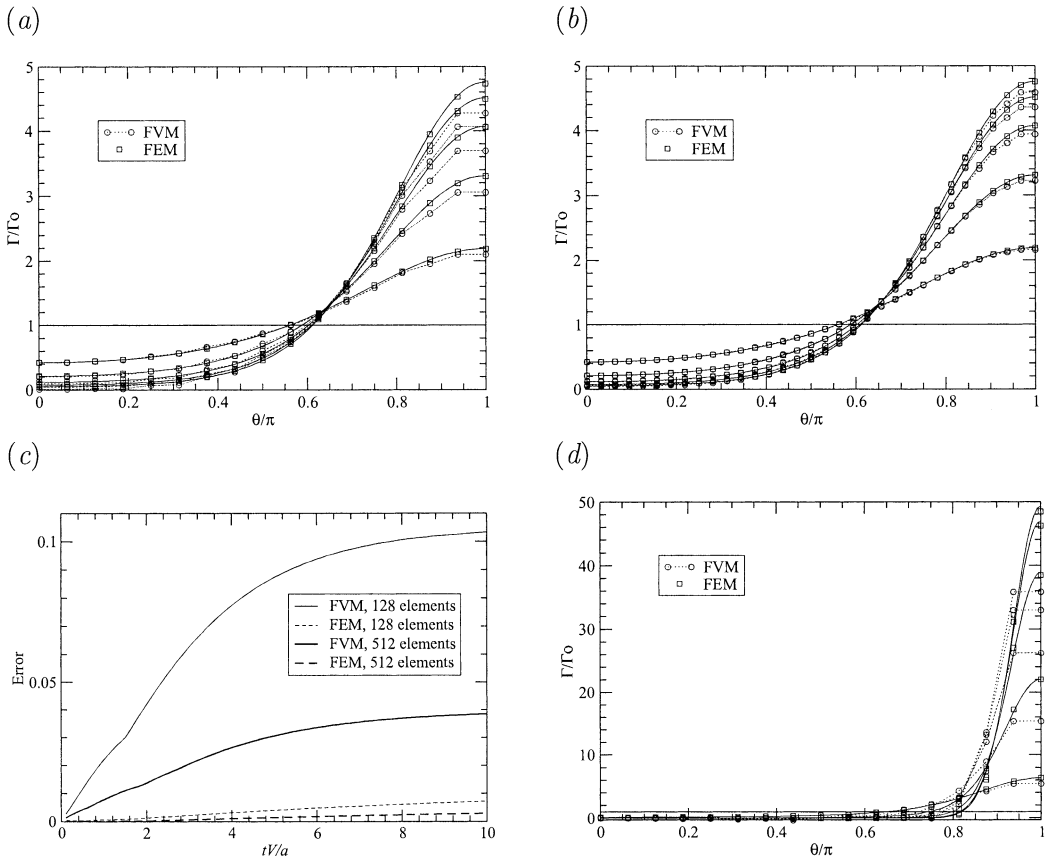

Figure 4. Comparison of the numerical methods for axisymmetric transport over a stationary spherical surface. In (*a, b, d*), the solid lines represent results obtained by solving (6.1) using an accurate finite-difference method, the squares correspond to the finite-volume method, and the circles correspond to the finite-element method on (*a, d*) a 128-element, and (*b*) a 512-element grid. In (*a, b*), Pe $= 10$, and in (*d*) Pe $= 100$. (*c*) Behavior of the maximum nodal error in the simulations shown in (*a, b*).

the evolution. In contrast, the finite-element method is remarkably accurate even when only three nodes are used to describe the transition zone around the sharp peak.

It is well known that the performance of the Galerkin finite-element method for the convection–diffusion equation worsens as the cell Péclet number, $\mathrm{Pe}_c \equiv hV/D_s = (h/a)\,\mathrm{Pe}$, becomes higher; in this definition, h is the designated element size (i.e., [10, p. 40]). For the coarse grid depicted on the right of Figure 3, having 32 nodes around the mid-plane, we take $h = 2\pi a/32$. The symbols in Figure 5 show the finite-element solution for Pe $= 1000$ corresponding to $\mathrm{Pe}_c = 196$, at dimensionless times $tV/a = 0, 1{\cdot}0, 2{\cdot}0, \ldots$. The solid lines show the corresponding numerical solution computed by the high-resolution finite-difference method. The onset of oscillations, confirmed to be independent of the size of the time step, is consistent with the well-known poor performance of the Galerkin finite-element method for convection-dominated transport. To circumvent this difficulty, Petrov-Galerkin methods and stabilization techniques can be used, as discussed by Donea and Huerta ([10, pp. 50–70]).

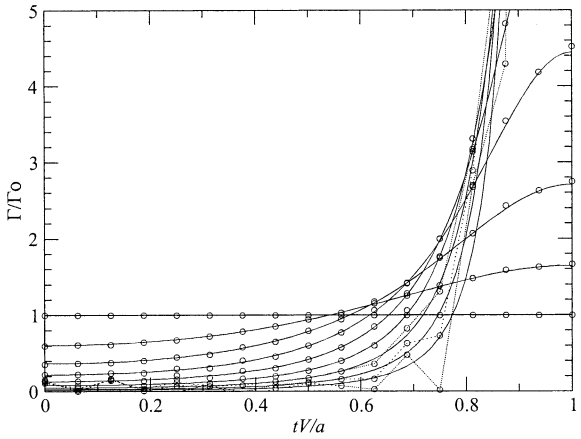

Figure 5. Onset of oscillations in the finite-element solution for convection-dominated transport.

6.2. DEFORMATION OF A VISCOUS DROP

As a second case study, we consider the deformation of an initially spherical liquid drop of radius a suspended in a virtually infinite ambient liquid undergoing simple shear flow along the x axis. Far from the drop, the unidirectional velocity field is given by $\mathbf{u}^{\infty} = (ky, 0, 0)$, where k is the shear rate. The interface between the drop and the ambient fluid is occupied by an insoluble surfactant, with the surface tension being a function of the local surfactant concentration according to an assumed equation of state.

The transient and long-time deformation of the drop depends on three dimensionless parameters: the ratio of the internal to the external fluid viscosities, λ, the capillary number $\mathrm{Ca} = \mu ka/\gamma_0$, and the property group $\alpha = a\gamma_0/(\mu D_s)$, where μ is the viscosity of the ambient fluid, and γ_0 is the surface tension of the undeformed spherical drop. Note that the property group α can be replaced by the surface Péclet number $\mathrm{Pe} = ka^2/D_s = \alpha\,\mathrm{Ca}$. In addition, the behavior of the drop depends on the relation between the surface tension and surfactant concentration, as determined by a surface equation of state.

In the numerical simulations, the equations describing the motion of the element nodes were integrated in time using the second-order Runge-Kutta method. For non-unit viscosity ratio, the node velocity was computed by solving an integral equation of the second kind over the instantaneous drop surface. The solution was found by a boundary-element method on the same interfacial grid used to define and advance the surfactant concentration (*e.g.*, [6].) For unit viscosity ratio, simplifications occur and the node velocity can be evaluated simply by computing a surface integral defining the Stokes flow single-layer potential. As soon as the velocity is computed at the beginning of a time step, the surfactant concentration is advanced using the Crank-Nicolson method, and the updated value is used for the second velocity evaluation at the end of the first Runge-Kutta sub-step. The maximum change in the drop volume due to numerical error was less than 0·5% through the length of each simulation.

Figure 6 shows results of simulations for fluids with equal viscosity, $\lambda = 1$, capillary number $\mathrm{Ca} = 0{\cdot}2$, property number $\alpha = 100$, and for a linear surface equation of state with $\beta = 0{\cdot}5$. These simulations were conducted with a fine grid of 512 surface elements described by 1026 nodes, and a reduced time step $k\Delta t = 0{\cdot}025$. Each time step requires approximately 15 sec of CPU time for advancing the marker point position using the second-order Runge-Kutta method, and an additional 4 or 30 sec for advancing the surfactant concentration by the

Crank-Nicolson method using, respectively, the finite-volume or finite-element method, on a 2·4 GHz processor. The lengthiest simulation involving 400 time steps requires 4 hr of CPU time.

Figure 6(*a*) shows the evolution of the Taylor deformation parameter, defined as $D = (L - B)/(L + B)$, where L and B are the maximum and minimum drop dimensions in the xy plane. Figure 6(*b*) shows the evolution of the drop inclination angle, θ, corresponding to the maximum dimension of the drop contour in the xy-plane. The dotted lines in these graphs describe the behavior for an inactive surfactant, corresponding to $\beta = 0$. The choice of method for solving the surfactant transport equation and policy of marker point motion is shown in the legend for the individual simulations. All computations show that, at long times, the drop tends to obtain an asymptotic equilibrium shape that is inclined at approximately 31° with respect to the x axis. The presence of the surfactant acts to promote the drop deformation and reduce the drop inclination. These results validate and confirm the consistency of the numerical methods. Although the finite-element method is somewhat more accurate than the finite-volume method, the advantages are not overwhelming. The dashed lines in Figure 6(*a*, *b*) correspond to simulations where the marker points are advanced with the interfacial fluid velocity. Because the surface grid is convected by the flow and suffers continuous distortion, numerical instabilities arise and the computation terminates at an early stage of the evolution.

Figure 6(*c*, *d*) shows the structure of the interfacial grid near the steady state. In the illustration presented in Figure 6(*c*), corresponding to time $kt = 10$, the interfacial marker points move with the normal component of the fluid velocity; in the illustration depicted in Figure 6(*d*), corresponding to time $kt = 6{\cdot}5$, the interfacial marker points move with the fluid velocity. The mild shading in these figures represents the surfactant concentration, with a hardly discernible darker color implying a higher concentration. These illustrations show that the surfactant accumulates at the tips, thereby lowering the surface tension, and is depleted from the waist of the drop due to convection, thereby raising the surface tension. The overall effect is a small increase in the drop deformation.

The squares and filled circles in Figure 6(*e*) show the node position in the xy-plane at time $kt = 5{\cdot}0$, for motion with the total or normal component of the fluid velocity. The high concentration of the squares near the tips is a reason for the impending numerical instability. Figure 6(*f*) shows the corresponding distribution of the surfactant concentration over the drop cross-section in the xy-plane. The surfactant distribution described by the finite-element method is notably smoother than that described by the finite-volume method for both types of marker point motion.

6.3. Effect of the surface equation of state

As a physical application of the numerical methods, we consider the effect of the surface equation of state on the deformation of a viscous drop. Since the effect of a surfactant is most noticeable for low-viscosity drops, we set the viscosity ratio to $\lambda = 0{\cdot}10$. The deformation of the drop was computed on the 512-element grid described by 1026 nodes using the boundary-element method discussed earlier in this section, with a time step $k\Delta t = 0{\cdot}0125$, for several hundred steps. For non-unit viscosity ratio, computing the interfacial velocity requires solving an integral equation of the second kind. Each time step requires approximately 2 min of CPU time for advancing the marker point position by the second-order Runge-Kutta method, and an additional 4 or 30 sec for advancing the surfactant concentration using, respectively, the finite-

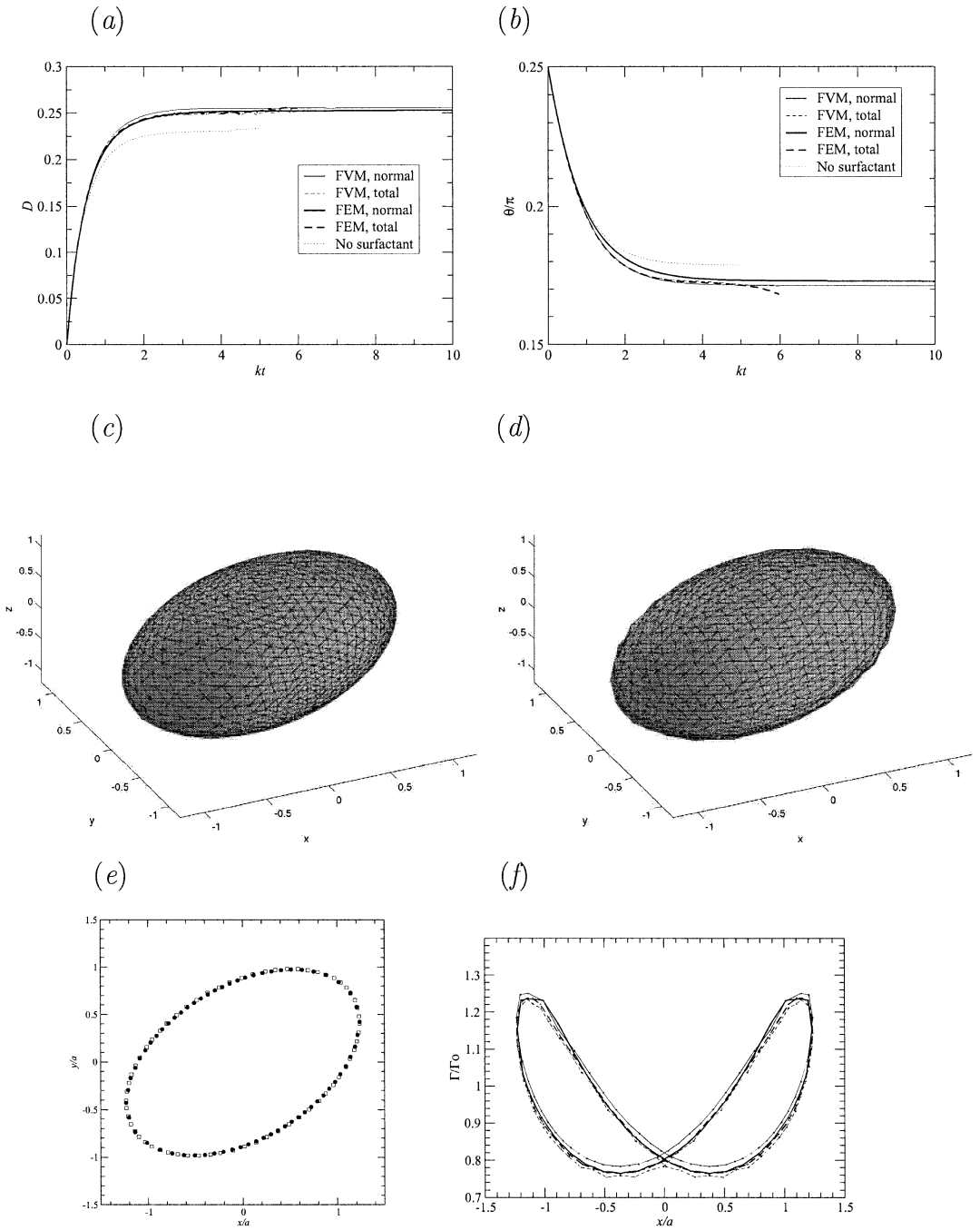

Figure 6. Deformation of a viscous drop for fluids with equal viscosity, $\lambda = 1$, Ca $= 0{\cdot}2$, $\alpha = 100$, and a linear surface equation of state with $\beta = 0{\cdot}5$. Evolution of (*a*) the Taylor deformation parameter, and (*b*) the drop inclination in the xy plane. (*c*, *d*) Structure of the interfacial grid near the steady state when the marker points move with the normal component of the fluid velocity or with the total fluid velocity. (*e*) Distribution of the nodes, and (*f*) corresponding distribution of the surfactant concentration in the xy plane at time $kt = 5{\cdot}0$.

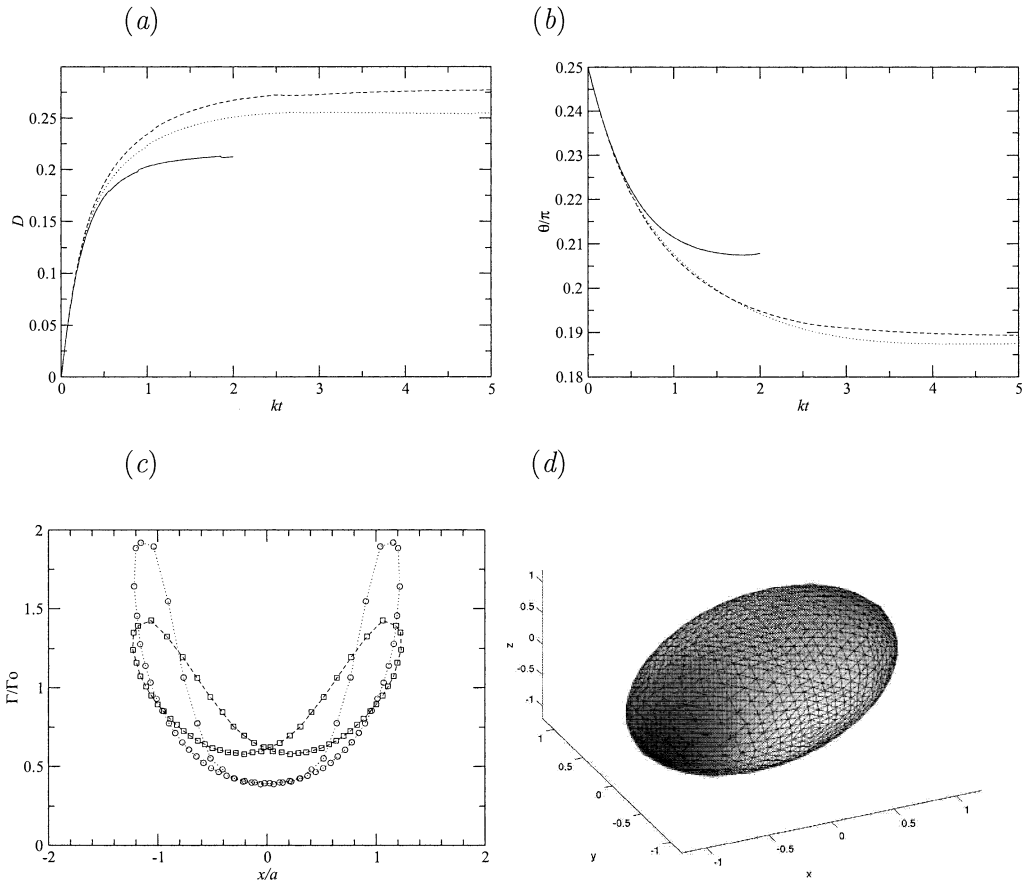

Figure 7. (*a, b*) Deformation of a low viscosity drop, $\lambda = 0.10$, for Ca $= 0{\cdot}2$ and constant surface tension (solid lines), linear surface equation of state with $\beta = 0{\cdot}20$ (dotted lines), or the Langmuir surface equation of state with $\beta = 0{\cdot}20$ and $\psi = 0{\cdot}50$ (dashed lines). (*c*) Distribution of the surfactant concentration in the xy plane for the linear equation of state (circles connected by the dotted line), and the Langmuir surface equation of state (squares connected by the dashed line). (*d*) Structure of the interfacial grid near the steady state for the linear equation of state.

volume or finite-element method on a 2·4 GHz processor. The lengthiest simulation involving 400 time steps requires 17 hr of CPU time.

Figure 7(*a, b*) shows the evolution of the Taylor deformation parameter and drop inclination for Ca $= 0{\cdot}20$, and an interface with constant surface tension (solid lines), the linear equation of state with $\beta = 0{\cdot}20$ (dotted lines), and the Langmuir equation of state with $\beta = 0{\cdot}20$ and $\psi = 0{\cdot}50$ (dashed lines). In the case of variable surface tension, $\alpha = 100$. The results show that the surfactant equation of state has a significant effect on the drop deformation. In particular, a drop with a Langmuir interface deforms more than of a drop with the Henry interface, although it is inclined at a slightly lesser angle. The significant effect of the surface equation of state is illustrated more clearly in Figure 7(*c*), showing the distribution of the surfactant concentration in the xy plane for the linear equation of state (circles connected by dotted line), and the Langmuir surface equation of state (squares connected by the dashed line). Figure 7(*d*) depicts the structure of the interfacial grid near the steady state for the linear equation of state, shaded so that dark regions correspond to high surfactant concentration.

7. Discussion

An arbitrary Lagrangian-Eulerian finite-element method has been developed for solving the transport equation of an immiscible surfactant over a stationary or evolving interface described by an unstructured grid. Numerical testing has suggested that the method performs generally better than a particular implementation of the finite-volume method developed in previous work, where performance is measured by accuracy for a certain level of spatial discretization. One drawback of the finite-element method is that it requires solving a linear system whose size is equal to the number of nodes, which is nearly twice the number of quadratic elements. In contrast, the size of the linear system arising from the finite-volume method is equal to the number of elements. However, the computational cost can be reduced by using linear solvers specifically designed for finite-element applications.

An alternative comparison between the two methods would consider differences in performance for the same degrees of freedom, that is, for the same size of the linear systems originating from the finite-volume or finite-element formulations. However, in the case of axisymmetric transport, the accuracy of the numerical solution in both cases depends on the number of azimuthal divisions, which is determined by the total number of elements and not by the total number of nodes. In fact, the results presented in Figure 4(c), show that the finite-volume solution with 512 elements (degrees of freedom) defined by 1026 nodes, is less accurate than the finite-element solution with 128 elements defined by 258 nodes (degrees of freedom.) Moreover, for the applications we have in mind, the level of discretization is dictated by specifications on spatial resolution and hydrodynamics.

In this paper, the Galerkin finite-element method was compared with *one particular implementation* of the finite-volume method described in Section 4. However, given the flexibility of the latter, it is possible that other implementations can be designed to improve the accuracy, for example, by better resolving regions of accumulation and boundary layers. These observations, along with the conservative properties of the finite-volume method, underline the notion that the successful choice of a method is not universal but depends on the particular application.

Straightforward generalizations of both methods can be made to include the effect of surfactant solubility, implemented by incorporating an additional flux term on the right-hand side of the surface transport equation. The bulk surfactant concentration is governed by a convection–diffusion equation and is subject to a mixed interfacial condition that arises by setting the diffusive flux equal to the flux due to a prescribed kinetics. An integrated methodology that combines the hydrodynamics, the surface, and the bulk transport components has not been implemented except in special cases where convection is not important in the bulk of the flow [12]. This important computational development will be considered in future work.

Acknowledgements

The manuscript benefited from insightful reviews by the referees. This research has been supported by a grant provided by the National Science Foundation.

References

1. C. Pozrikidis, Effect of surfactants on film flow down a periodic wall. *J. Fluid Mech.* 496 (2004) 105–127.
2. M. Blyth and C. Pozrikidis, Effect of surfactants on the stability of two-layer channel flow. *J. Fluid Mech.* Accepted (2004).
3. C. Pozrikidis, Numerical investigation of the effect of surfactants on the stability and rheology of emulsions and foam. *J. Eng. Math.* 41 (2001) 237–258.
4. R.V. Craster, O.K. Matar and D.T. Papageorgiou, Pinchoff and satellite formation in surfactant covered viscous threads. *Phys. Fluids* 14 (2002) 1364–1376.
5. X. Li and C. Pozrikidis, The effect of surfactants on drop deformation and on the rheology of dilute emulsions in Stokes flow. *J. Fluid Mech.* 341 (1997) 165–194.
6. S. Yon and C. Pozrikidis, A finite-volume / boundary-element method for flow past interfaces in the presence of surfactants, with application to shear flow past a viscous drop. *Comp. Fluids* 27 (1998) 879–902.
7. M. A. Drumright-Clarke and Y. Renardy, The effect of insoluble surfactant at dilute concentration on drop breakup under shear with inertia. *Phys. Fluids* 16 (2004) 14–21.
8. S. Popinet and S. Zaleski, Bubble collapse near a solid boundary: a numerical study of the influence of viscosity. *J. Fluid Mech.* 464 (2002) 137–163.
9. G.E. Karniadakis and S.J. Sherwin, *Spectral/hp Element Methods for CFD.* New York: Oxford Univ. Press (1999) 390pp.
10. J. Donea and A. Huerta, *Finite Element Methods for Flow Problems.* Chichester: Wiley (2003) 350pp.
11. A.W. Adamson, *Physical Chemistry of Surfaces.* Fifth Edition. New York: Wiley (1990) 777pp.
12. N.R. Gupta and A. Borhan, Capsule motion and deformation in tube and channel flow. In: C. Pozrikidis *Modeling and Simulation of Capsules and Biological Cells.* Boca Raton: Chapman & Hall /CRC (2003) 333pp.
13. C. Pozrikidis, *Introduction to Theoretical and Computational Fluid Dynamics.* New York: Oxford Univ. Press (1997) 675pp.
14. C. Pozrikidis, *Numerical Computation in Science and Engineering.* New York: Oxford Univ. Press (1998) 627pp.
15. J.W. Demmel, *Applied Numerical Linear Algebra.* Philadelphia: SIAM (1997) 419pp.
16. C. Pozrikidis, *A Practical Guide to Boundary-Element Methods with the Software Library BEMLIB.* Boca Raton: Chapman & Hall /CRC (2002) 423pp.